Feasibility of diffusion weighting with a local inside-out nonlinear gradient coil for prostate MRI

Enamul H. Bhuiyan[1], Andrew Dewdney[2], Jeffrey Weinreb[1], Gigi Galiana[1]

[1]Department of Radiology and Biomedical Imaging, Yale School of Medicine, USA.

[2]Siemens Healthcare, Erlangen, Germany.

Version typeset September 22, 2020

Corresponding Author. email: gigi.galiana@yale.edu, Gigi Galiana, Associate Professor, Radiology and Biomedical Imaging, Yale University, School of Medicine, Phone: +1-(203) 785-5052

Abstract

Purpose: Prostate cancer remains the 2nd leading cancer killer of men, yet it is also a disease with a high rate of overtreatment. Diffusion weighted imaging (DWI) has shown promise as a reliable, grade-sensitive imaging method, but it is limited by low image quality. Currently, DWI image quality is directly related to low gradient amplitudes, since weak gradients must be compensated with long echo times.

Methods: We propose a new type of MRI accessory, an "inside-out" and nonlinear gradient, whose sole purpose is to deliver diffusion encoding to a region of interest. Performance was simulated in OPERA and the resulting fields were used to simulate DWI with two compartment and kurtosis models. Experiments with a nonlinear head gradient prove the accuracy of DWI and ADC maps diffusion encoded with nonlinear gradients.

Results: Simulations validated thermal and mechanical safety while showing a 5 to 10-fold increase in gradient strength over prostate. With these strengths, lesion CNR in ADC maps approximately doubled for a range of anatomical positions. Proof-of-principle experiments show that spatially varying b-values can be corrected for accurate DWI and ADC.

Conclusions: Dedicated nonlinear diffusion encoding hardware could improve prostate DWI.

Keywords: Diffusion weighted imaging (DWI), apparent diffusion coefficient (ADC), nonlinear gradient, prostate cancer, system design

i

I.   Introduction

I.A.   Prostate DWI

The lifetime risk of being diagnosed with prostate cancer is approximately 1/9 for American men[1–3], but because of slow progression and the significant morbidities associated with treatment, many men should consider declining, or at least delaying, treatment[4,5]. On the other hand, prostate cancer remains the 2nd leading cancer killer of men (following only lung cancer), so early detection of aggressive cancers remains an urgent problem. Therefore, one of the greatest needs in prostate cancer is a monitoring method that distinguishes benign or low grade prostate lesions from aggressive ones. Standard template biopsy, which blindly samples 10^+ cores in a regular pattern, risks overdiagnosis, underdiagnosis, and urinary and erectile dysfunction, making it a poor option for diagnosis or surveillance[6,7].

Diffusion-weighted MR imaging (DWI) does noninvasively detect prostate cancers[8–10] and the images can be quantified into maps of apparent diffusion coefficient (ADC), which consistently reflect Gleason score and aggressiveness. Therefore, DWI has potential to specifically improve the detection of deadly cancers. Brightness in a DWI image (or darkness in an ADC map, with inverted contrast) reflects restricted water diffusion, so it is sensitive to the decreased luminal space and increased epithelial volume that accompanies malignancy. For men with high PSA (prostate specific antigen), prior MRI, typically can reduce unnecessary biopsies by a third[11]. In addition, these images can be used for biopsy guidance, increasing detection of high grade cancer and reducing biopsies of low grade disease[12–15]. However, clinical adoption has been limited by the poor image quality observed in routine prostate DWI, which is a key part of the multiparametric protocol. Fig. 1 shows typical image quality from a prostate imaging protocol. While the structural T2w image (Fig. 1a) has good SNR and resolution, it shows little contrast between cancerous and benign tissue. This is not uncommon for peripheral zone lesions, which make up $\approx 75\%$ of cancer cases[8]. The ADC map (Fig. 1b), though very noisy and low resolution, does show markedly lower ADC in what was later confirmed to be an aggressive lesion. However, it was initially misread as artifact, due to the poor image quality. Images like these result in inconsistent interpretations, with high interreader variability, and limited clinical deployment[16].
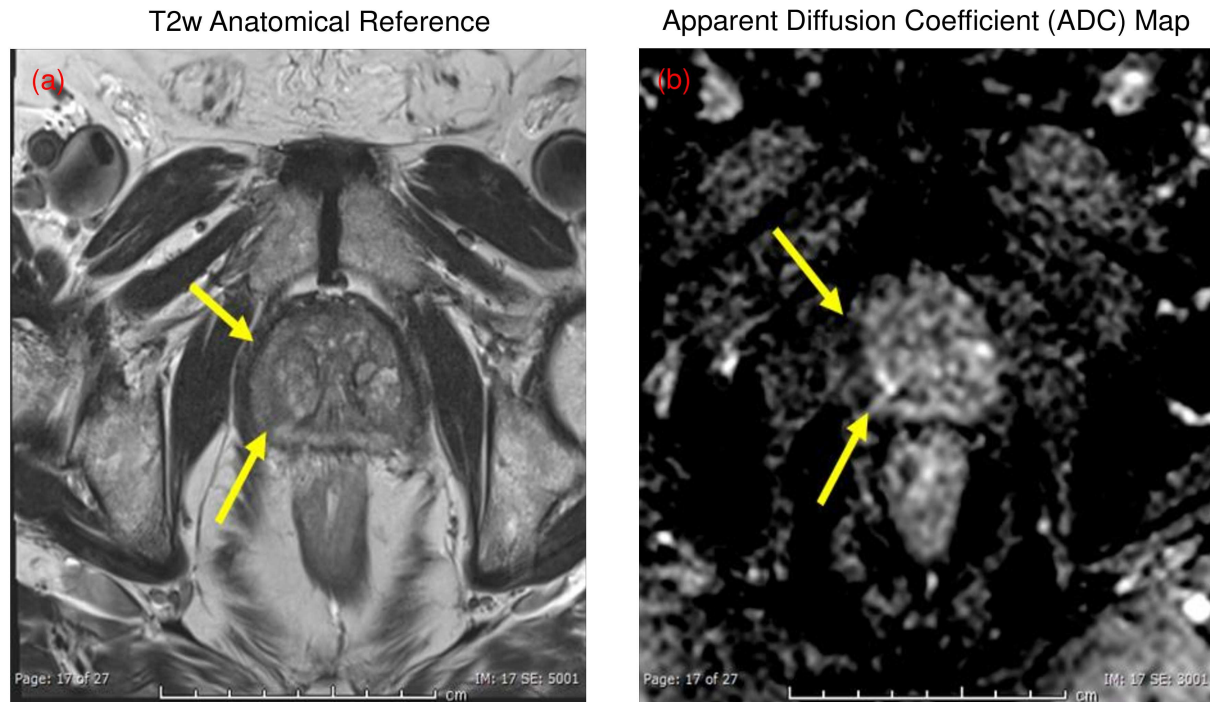
Figure 1: Images from a typical prostate MRI underscore the need for better imaging. (a) While a T2w image has high signal and resolution, it often fails to show contrast for peripheral zone tumors, which make up $\approx 75\%$ of cases. (b) In the same patient, a hypointense region in the ADC map (i.e. a region of low diffusion) does distinguish the cancerous region from healthy prostate. But the overall image quality is low due to the low SNR of conventionally encoded diffusion MRI. Because of these shortcomings in prostate imaging, most clinicians rely on blind biopsies of the prostate, which can lead to over- and under-diagnosis of lethal disease.

Prostate DWI images are noisy because diffusion weighting depends exponentially on the square of gradient strength, and limited gradient strength must be compensated for by applying the gradient for very long times. The most widely used and simplistic model of diffusion is for Gaussian unrestricted diffusion, where:

$$S_{DWI} \approx S_0 e^{\left(-D\gamma^2 G^2 \delta^2 (\Delta - \frac{\delta}{3})\right)} \equiv S_0 e^{(-Db)}, \tag{1}$$

where S_{DWI} and S_0 are the signal intensities with and without diffusion weighting, respectively, D is the intrinsic diffusion rate of the spins, analogous to the apparent diffusion coefficient (ADC) observed in vivo, γ is the gyromagnetic ratio, G is the local gradient

74 amplitude, and Δ and δ are timings related to the duration of the gradient pulses which
75 contribute to the overall echo time (TE)[17,18]. The known experimental parameters in this
76 expression are typically grouped together as a single measure of diffusion weighting, b. Using
77 standard clinical gradients, strong diffusion weighting requires echo times of $\approx$ 100ms, during
78 which signal decays precipitously. Furthermore, long TE overemphasizes the luminal volume
79 of the prostate, which reduces contrast between aggressive and benign tissues. Empirical
80 studies on the impact of TE and diffusion encoding time have shown that shorter encoding
81 times and higher b-values increase the ability to distinguish between benign and cancerous
82 lesions[19–24]. The need for gradients that can deliver strong diffusion weighting in short times
83 motivated the search for alternative possibilities in gradient design.

84 I.B.   Nonlinear Gradients

85 Existing gradient hardware generates a Bz magnetic field whose magnitude changes linearly
86 with position (Fig. 2a, red line), so the local field slope or gradient is uniform across
87 the field of view. Nonlinear gradients similarly generate a Bz whose magnitude varies in
88 space (Fig. 2a, blue line), but the magnitude and direction of the field slope is different at
89 different locations[25–28]. Put another way, for a given Bz, linear gradients distribute gradient
90 amplitude ($\| \nabla Bz \|$) with perfect equality to all positions in the field of view (FOV). (Fig.
91 2b) A comparable nonlinear gradient, by mathematical necessity, concentrates the gradient
92 amplitude, leaving some regions with almost no gradient, but in other regions providing
93 much higher gradient. For example, in the theoretical example of Fig. 2, a significant region
94 in the field of view receives > 5 times the gradient strength of the comparable linear gradient
95 field.

96   This insight can be used to design hardware that efficiently generates very strong gra-
97 dients in a particular anatomy of interest. For the targeted region of interest, the strong
98 gradients deliver strong diffusion weighting in a short encoding time, thereby increasing sig-
99 nal to noise ratio (SNR) and contrast. On the scale of a voxel or the distance travelled by
100 a diffusing spin, the field change remains approximately linear, so the same equations are
101 applicable, except that gradient strength varies from voxel to voxel. This approximation has
102 been confirmed by both experiments (Fig. 7 and Fig. 8) and first principles derivations (see
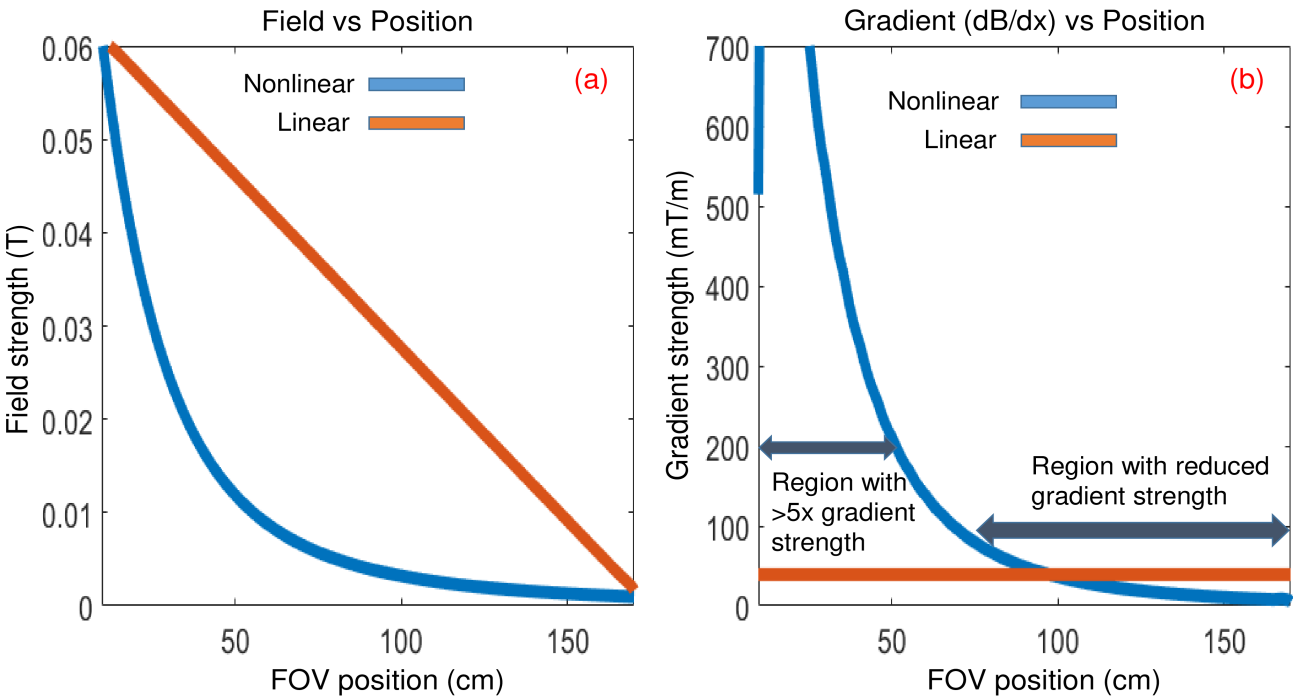
Figure 2: Conceptual schematic showing the inherent advantages of linear vs nonlinear field variations. For a maximum $\| Bz \|$ of 60mT over this FOV (2a), linear gradients provide all points with the same gradient strength (2b) of 36mT/m. A nonlinear gradient with the same maximum $\| Bz \|$, by mathematical definition, provides less gradient in some regions but more gradient in others. For part of the field of view, this results in a much stronger gradient that can be used to impart diffusion weighting. In practice, the advantages of a nonlinear diffusion gradient are even greater, including fewer cancellations which would normally be needed to achieve linearity and potential for "inside-out" single-sided gradient designs.

103   APPENDIX I).

104   Designing a gradient specifically for diffusion weighting, rather than repurposing hard-
105   ware primarily designed for spatial encoding, brings additional advantages for increasing
106   gradient strength. The usual requirements on slope uniformity, both in magnitude and di-
107   rection, require many field cancellations which ultimately waste amplifier energy. Reducing
108   the volume over which the field must be generated may also reduce power needs[29].

109   In fact, nonlinearity allows for hardware designs that do not encompass a volume at
110   all, like the one presented here. Finally, since diffusion weighting requires just a few ramps
111   per TR, short rise times are less critical. This allows higher inductance, more turns and
112   therefore more field per amp. Alternatively, less voltage is required to achieve the slew rate,

which reduces requirements on the amplifier and lowers the voltage breakdown strength requirements in the gradient coil[29,30]. Linear gradients, which can provide fast switching times and homogeneous spatial encoding over the entire FOV, can still be used for the rest of the pulse sequence, including slice selection, frequency and phase encoding, or any kind of preparation module. Therefore, standard DWI pulse sequences can be modified by simply adding a synchronization pulse that turns the nonlinear gradient on and off during diffusion encoding time. Notably, the nonlinear gradient can be played simultaneously with linear gradients, either for spatial encoding purposes like a prephaser, or to further add to the diffusion encoding gradient. When the spatial encoding is done by conventional means, the reconstruction is similarly conventional and can use regular FFT.

I.C.   Nonlinear Gradients for Prostate DWI

Anatomically, DWI encoding with nonlinear gradients (NLG) is most naturally suited to an organ that is (i) small, so that each experiment yields an acceptable range of b-values across the region of interest (ROI), (ii) close to an accessible surface of the body, since gradients are typically strongest near the device, and (iii) structurally isotropic, so that variation in gradient direction is not a major confound. In practice, to justify additional hardware, the DWI contrast would also need to be a critical image for diagnosis. Thus, prostate cancer imaging is an ideal initial target for this type of hardware. The prostate is a small 4cm organ located only $\approx$ 6cm from the perineal surface with relatively isotropic diffusion, and prostate cancer is a widespread and deadly disease which is best imaged by DWI MRI. Furthermore, prostate MRI is a rapidly growing application, as it is increasingly recognized as a cost-effective step following elevated PSA[31–37]. Therefore, this was chosen for a first and ideal organ to benefit from this class of device.

Putting these insights together, we designed an inside-out gradient that provides very high diffusion weighting at the prostate. Standard gradient hardware is generally built into a volume-encompassing former, typically a tube-like shape, and the relevant fields are generated inside the volume of the hardware. In contrast, nonlinear gradients windings can be placed in a wand-type former, generating the relevant fields outside the hardware. The proposed device has a diameter of 10cm, comparable to a typical coffee mug, and can be placed between the upper thighs to achieve close proximity to the prostate. (Fig. 3) This

143 geometry also minimizes interference with the standard linear gradients, which can be used
144 for spatial encoding in the usual way, and standard receiver geometry, which is typically a
145 set of anteriorly and/or posteriorly positioned surface coils.
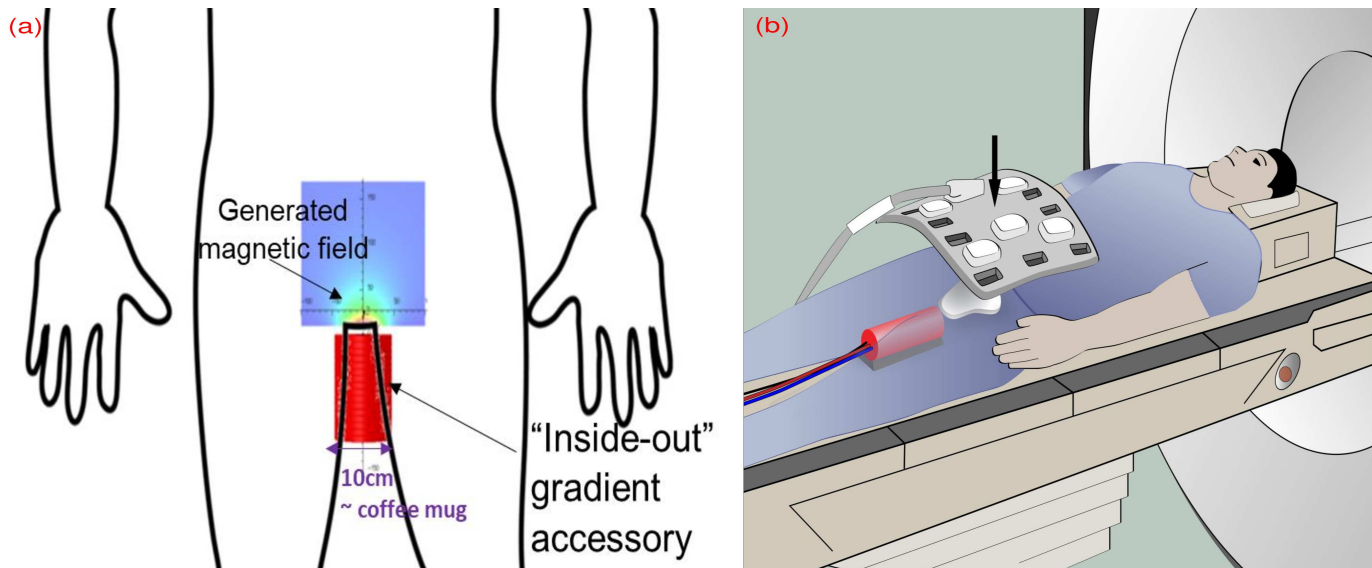
Figure 3: Positioning logistics for proposed hardware. Panel (a) shows general device placement and an overlay of the generated field. Panel (b) shows positioning in the scanner along with placement of a flex receive array. The gradient is placed externally, posterior to the genitalia and anterior to the anus, which provides close proximity to the prostate.

146 II.   Methods

147 II.A.   Simulations

148 From analyses of body MRI scans, the prostate is approximately a 4cm sphere whose lower
149 edge is 6cm superior from the perineal surface.The presented prototype was designed by
150 Tesla Engineering Ltd and simulated using OPERA Electromagnetic Simulation Software
151 (Oxfordshire, UK). This design was then analyzed by Siemens Healthcare GmbH for whole-
152 body forces and coupling effects with the Siemens superconducting magnet and gradient coils
153 of a MAGNETOM Prisma with in-house software. All imaging simulations are performed
154 in Matlab assuming a two compartment model comprised of a luminal compartment and
155 a joint cellular and epithelial compartment. Parameters taken from[20–23] were used to set:

T2$_l$=250ms, T2$_c$=50ms, D$_l$=2.5μm^2/ms, D$_c$=1.3μm^2/ms. Recent studies suggest the main driver of increased ADC with malignancy is loss of the luminal compartment volume, so this fraction was varied as 30%, 15% and 7% for healthy prostate, medium grade prostate cancer in a lesion on the left, and aggressive prostate cancer in a lesion on the right, respectively[24].

The multicompartment model introduced nonmonoexponential signal behavior observed clinically, both in the signal as a function of b and in ADC as a function of echo time. However, as done clinically, the resulting signal as a function of b was fit to a simple monoexponential to create maps of ADC. Since these experiments are meant to model the commonly used spin echo DWI sequence with $\Delta < 100$ms, rather than a STEAM sequence, the impact of Δ on ADC was neglected. While 80mT/m gradients are now available commercially, these are often associated with very expensive and comprehensive upgrades. Thus we have performed comparisons against the more commonly available 40mT/m gradient strengths.

Simulated ADC maps were generated using b-values of 60, 600, and 1500 for linear gradients and a maximum gradient strength of 40mT/m. For nonlinear gradients, diffusion gradient duration was chosen according to the prostate position in the FOV so that the least encoded pixel in prostate achieved a b value of 400. Diffusion weighted images were then simulated for 20%, 45%, 75% and 100% gradient strength. The highest b-values used for ADC calculation were 3000. Diffusion values higher than this were sometimes induced in the 4th DWI image for pixels very close to the device, but in this case the first 3 DWI images were sufficient for ADC calculation. Studies of position used a noise power of 15.

Simulations were also performed for a model of diffusion which includes kurtosis, with T2/D/K equal to 130ms/1.89μm^2/ms/0.63 and 80ms/1.41μm^2/ms/1.19 for healthy and cancerous prostate tissue, respectively. In these simulations, images were simulated for gradient strengths of 20, 30, 40, 55, 70, 85, 100% maximum amplitude for both linear and nonlinear gradients, and noise power was reduced to 5. Durations were set to achieve a maximum b-value of 3000 in the linear experiment and a minimum b-value of 500 in the nonlinear experiment.

Due to the spatially varying b-value in nonlinear experiments, the raw data from these scans also exhibits spatially varying contrast and spatially varying SNR. While the nonlinear scans can be used to make DWI with uniform b-value (as shown in Fig. 7), the fidelity of those images is ultimately determined by the fidelity of the ADC map used for scaling. Therefore,

as an equitable metric to compare nonlinear and linear experiments, we calculated CNR in ADC maps as: $(\mu(\text{ADC}_{lesion})\text{-}\mu(\text{ADC}_{normal})/(\sigma(\text{ADC}_{normal})^2 + \sigma(\text{ADC}_{lesion})^2)^{1/2}$, where μ is the mean and σ is the standard deviation over each ROI. In simulations, since the exact delineation of healthy prostate and lesions were known, these were used as the ROIs for each tissue type.

II.B.   Experiments

To prove the feasibility of encoding diffusion with a nonlinear gradient, initial experiments were performed with an existing nonlinear gradient, a volume encompassing head coil that produces a "C3" field shape $Bz(x,y) = x^3 - 3xy^2$. These studies imaged a kiwi, which has been lauded as a highly concordant phantom for prostate DWI[38], embedded in gelatin and a nominal gradient strength of 816, 1632, and 2449mT/m³ with TE=32ms and gradient duration of 12ms. The linear experiments on this phantom used strengths of 10, 20, and 30mT/m with TE=60ms and gradient durations of 26ms. All experiments were acquired with a 1-channel Tx/Rx head coil nested inside the existing nonlinear gradient insert. In nonlinear gradient studies, scaling to a uniform b-value was performed by using raw data with acquired b-values to generate an ADC map and then extrapolating, via a monoexponential fit, to the desired b-value[39].

Additional experiments were performed on a High Precision Device (HPD) diffusion phantom Model 128 containing thirteen 30ml vials of the nontoxic polymer polyvinylpirroli-done (PVP) in aqueous solution having different concentrations of PVP[40,41]. As the ADC depends on temperature, it is necessary to maintain a constant temperature in order to achieve reproducible ADCs. Coexistence of ice and water in the phantom serves to maintain temperature at 0°C. Because b-values from NLG encoding vary substantially over this rela-tively large phantom, gradient durations that achieved reasonable diffusion weighting for one vial would provide too much or too little diffusion weighting in another vial. Furthermore, regions far from the bore periphery have very little diffusion weighting even at long gradient durations. Instead, across a series of studies with increasing gradient duration, we identified, for each vial, the study where the maximum b-value averaged across the ROI was closest to a target value of 1500. ADC for the region was then calculated using that experiment and compared to the result from a conventional DWI experiment using linear gradients. Linear

experiments on this phantom used TE=61ms, gradient lobes of 26ms, and gradient strengths as in the kiwi experiment. NLG experiments used TE=26-98ms with gradient durations of 14-38ms and gradient strengths as in the kiwi experiment.

Field mapping was performed by incrementing the duration of a single gradient lobe (1.5-2ms) at low amplitude to avoid intravoxel dephasing, holding TE fixed at 20ms. The observed phased progression was used to calculate local frequency as $\omega(x,y) = \Delta\Phi(x,y)/\Delta t$, and this was used to generate a map of the static field, which was then masked and fit to ta polynomial to generate a field map across the entire FOV. The local gradient was calculated as $(G_x(x,y)^2 + G_y(x,y)^2)^{\frac{1}{2}}$, and this was used to calculate the b-values for each voxel. To control for any differences in processing, linear gradients and b-values were calculated by the same procedure, but high uniformity and agreement with the nominal field was observed, as expected.

For imaging in these proof-of-principle experiments, a 2D GRE sequence with bipolar diffusion encoding gradients was used with the following parameters, FOV=250×250mm^2, matrix size 256×256, TR=500ms, 500Hz/pixel receiver BW, flip angle 50°. All experiments used standard gradient echo sequences with Cartesian trajectories played out on linear gradients and bipolar diffusion encoding gradients. The only difference between experiments was whether the diffusion encoding pulses were delivered on the linear vs nonlinear gradient hardware. All experiments were performed on a 3T Siemens Trio system.

III. Results

III.A. Simulation of Hardware Performance

Fig. 3a shows the general positioning and the field generated by the device, and Fig. 3b shows a mock-up of the device placed on the scanner bed. A patient would be positioned with the device externally nestled between the legs, and a receiver coil would be placed above these. Water and power cables would extend in the foot direction.

Simulations were also performed on this design to assess thermal and mechanical properties. Because the device is designed for placement at isocenter in the homogeneous region of the magnet, net forces due to device operation are expected to be negligible. Even for

245 misplacement up to ±1cm, forces are less than 1N due to symmetry. Even in a maximally

246 catastrophic case of complete symmetry loss at 100% current, forces on the device reach

247 < 500N, which can be restrained with adequately designed scaffolding. Improper position-

248 ing could also affect image quality through coupling to the linear gradients, but preliminary

249 analysis indicates that a positioning tolerance of ±2mm is both sufficient and achievable.

250 The device is cooled and insulated such that surface temperature at maximum duty cycle

251 will not exceed 42°C. Other key metrics are reported in Table 1.

Gradient Specifications	
Diameter	94mm
Length of active section	110mm
Total length	170mm
Resistance	$37\mu\Omega$
Inductance	$305\mu H$
Peak Current	625A
Peak Voltage	500V
Steady state DC current	550A
Dissipation at max DC current	13kW
Pressure Drop	0.68bar
Parallel water circuits	8
Flow rate	8.8 L/min
Water inlet temp	20°C
Maximum temperature	42°C

Table 1: Summery of the key metrics

252 Fig. 4 shows the generated field predicted for this design for a coronal plane assuming a

253 625A 500V amplifier, showing both the z-component of the gradient (4a) and the component

254 in the transverse plane (4b). The device and field exhibit cylindrical symmetry about the

255 z-axis. The typical expected position of a prostate is outlined in red. Putting these together

256 as G_{tot} (4c), it can be seen that the total gradient magnitude varies mostly as a function

257 of z (i.e., the head-foot direction). Therefore, gradient is plotted as a function of z in 4d,

258 focusing on the ROI of a typical prostate. Fig. 4e shows a contour plot of b-values for a 1ms

259 pulse at full current. The overall topology of this plot is that of G_{tot}^2, and the values scale

260 uniformly with the square of amplifier power. Minimum rise times to maximum current are

III. RESULTS   III.A.   Simulation of Hardware Performance
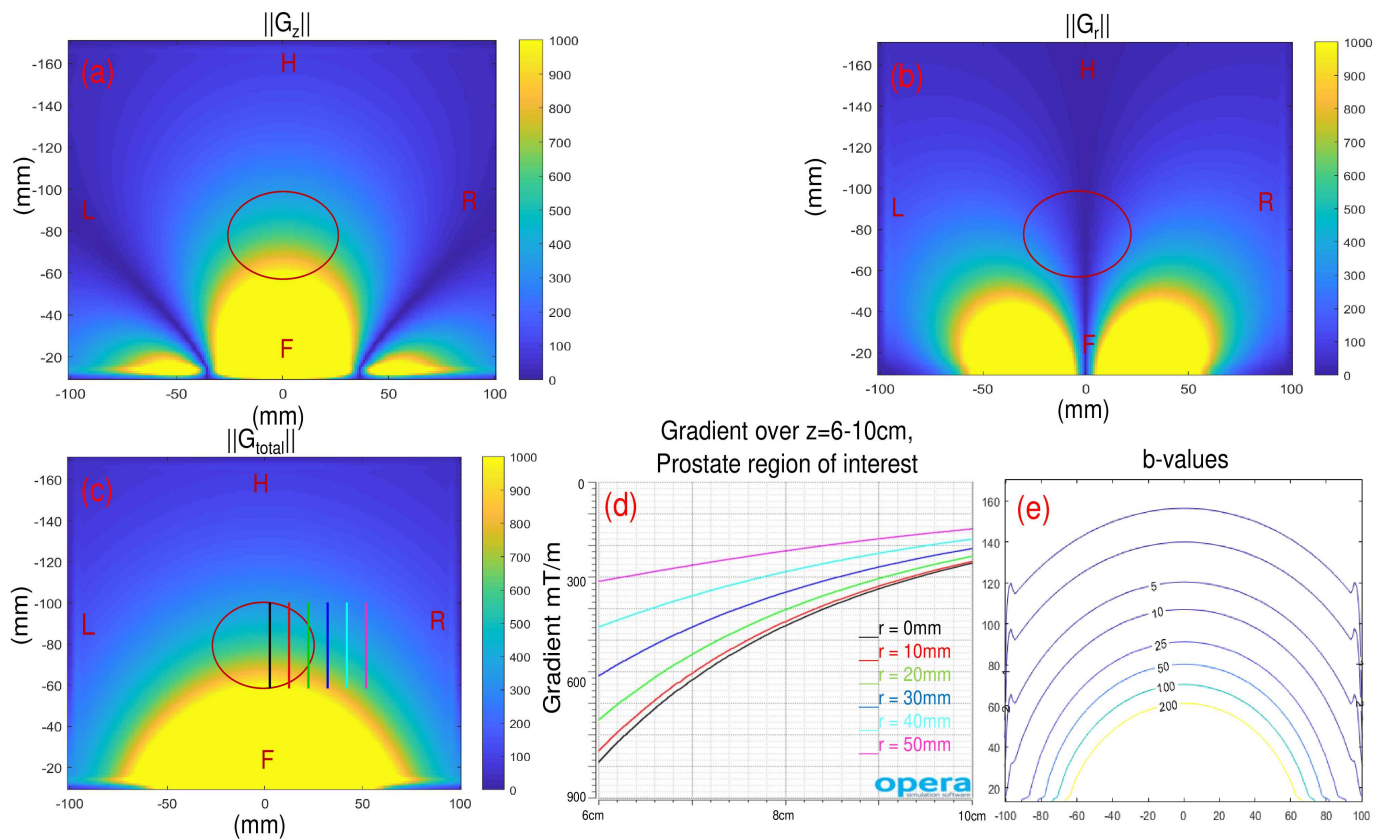
Figure 4: Images of gradient strength across the field of view. (a,b) Field variations in both the head-foot (a) and left-right direction (b) contribute to diffusion encoding. Summing these, the overall gradient magnitude (c) varies primarily along the head-foot direction. In each figure, the red outline shows the typical position of the prostate at closest approach. Various traces in the total gradient and a map of b-values are plotted in (d) and (e), respectively.

261 397μs, though practical rise times would depend on peripheral nerve stimulation, as further

262 considered in Discussion.

263 III.B.   Simulation of ADC Map Improvement

264 Fig. 5 shows simulations of the potential image improvements from implementing such a

265 gradient. Because SNR and b-weighting vary spatially in images acquired with nonlinear

266 gradients, standard DWI images would require scaling via an ADC map, so analyses focus

267 on these.
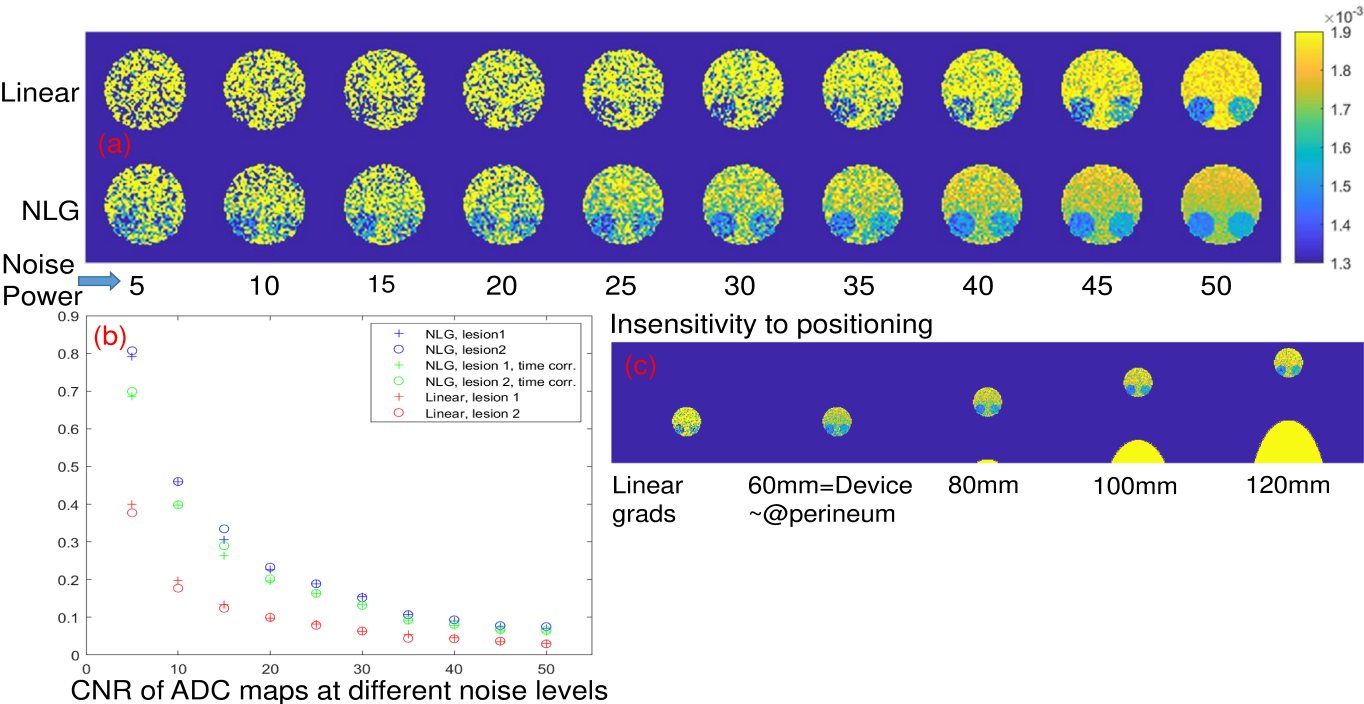
Figure 5: CNR of ADC maps simulated for diffusion encoding with linear and nonlinear gradients. (a,b) As expected, at the lowest noise levels, lesions are identifiable even with the longer echo times needed by linear gradients. However, the shorter echo time used with nonlinear gradients ultimately results in a consistent doubling of CNR in ADC maps. (c) With nonlinear gradients, position of the prostate relative to the hardware could potentially affect performance, as a longer diffusion time is required to achieve sufficient weighting. However, simulations show that this dependence is relatively minor, and CNR remains well above that observed with linear gradients.

	Linear gradient	Nonlinear Gradient			
Position (mm)	60	60	80	100	120
CNR, Lesion 1	100% (ref)	200%	230%	210%	190%
CNR, Lesion 2	100% (ref)	200%	230%	210%	190%
Time corr. CNR Lesion 1	100% (ref)	175%	200%	180%	165%
Time corr. CNR Lesion 2	100% (ref)	175%	200%	180%	165%

Table 2: CNR insensitivity to position

268 Fig. 5a shows simulated ADC maps generated with linear and nonlinear gradients at
269 various noise levels. Fig. 5b, summarizes the contrast to noise ratios observed in each image
270 for the medium and high grade lesions. The proposed nonlinear gradient is associated with

271   a consistent doubling of contrast to noise over the standard method.

272   Fig. 5c simulates the effect of different positionings of the nonlinear gradient coil, mim-
273   icking either alternate placement or anatomy. The CNR improvements for these scenarios
274   are summarized in Table 2. While these studies do reveal a weak dependence of CNR on
275   position of approximately ±10%, all values are approximately a 2-fold improvement over the
276   contrast to noise ratio (CNR) achieved with linear gradients.

277   Fig. 6 explores the importance of these stronger gradients for higher b-value imaging
278   with greater SNR to fit kurtosis in a higher order model of diffusion[42,43]. For the high SNR
279   simulated in these experiments, the ADC maps are comparable in both cases. However, the
280   kurtosis maps show much better delineation of the lesions when using nonlinear gradients.
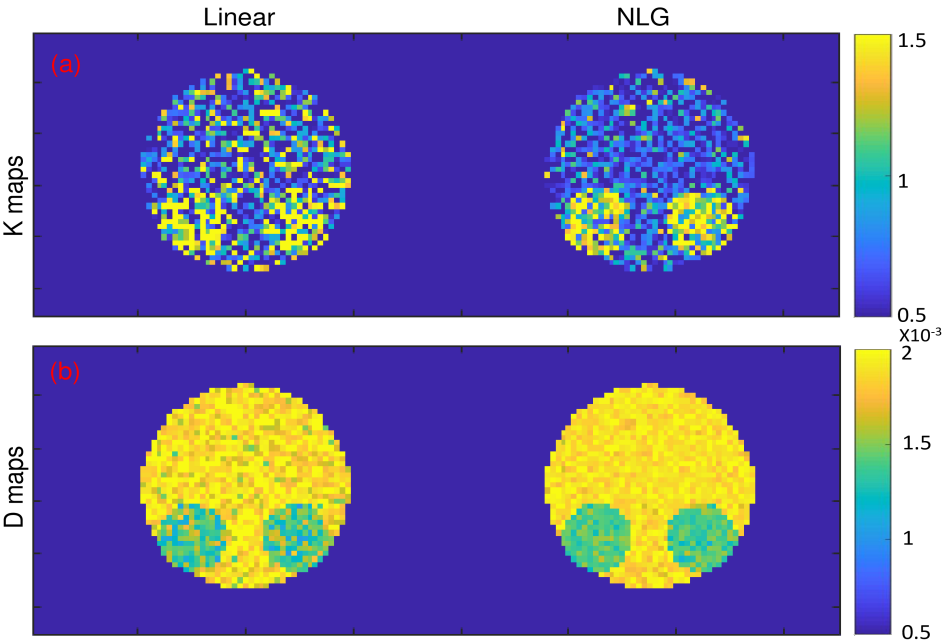
Figure 6: Fitting higher order models of diffusion. In this example, high b-value data was simulated with an additional second order term in the exponent of the standard diffusion model. The fit coefficient on this second order term is shown in (a), showing clearer delineation of the lesions with the NLG hardware. In these relatively low noise simulations, both ADC maps clearly delineate the lesion.

III.C. Experimental Demonstration of DWI with NLG

One key to achieving an order of magnitude increase in gradient strength is accepting nonlinearity in the field, which introduces nonuniform diffusion weighting across the image and could theoretically introduce bias in an ADC map. Thus we sought to show initial feasibility of DWI with nonlinear gradients using nonlinear gradient hardware available at our center[44–48]. Though the geometry of this device is not suitable for prostate imaging, the degree of nonlinearity is comparable and these results provide proof of principle demonstrations for encoding diffusion with a nonlinear field.

Fig. 7 shows individual diffusion weighted images acquired with nonlinear (7a) and linear (7b) gradients. To generate the images in 7a, the raw images must be scaled to a uniform b-value in the same way that low b-value images are routinely scaled to higher b-value images in clinical practice[39]. The raw images acquired with nonlinear gradients (7c) exhibit the spatial nonuniformity in diffusion weighting (blue arrows). As can be seen by comparing 7a to 7c, standard b-value scaling corrects this variability while maintaining improved SNR from the reduced TE. Parameter maps generated from fitting the data to a monoexponential signal model show good agreement in the ADC maps (7d,e). The fit to S_0 (7f,g) reflects the much higher signal achieved in the nonlinear gradient study. Though these proof-of-concept experiments do not use gradients optimized for this sample or positioning and employ $\approx$half the amplifier current, DWI with nonlinear gradients required less encoding time for comparable diffusion weighting across this phantom. This led to a doubling in signal, which is reflected in the maps of S_0.

To further explore the importance of the additional SNR associated with shorter echo times, the ROIs shown in panel (h) were used to assess image homogeneity over presumably homogeneous regions in both ADC maps and DWI images. These results, shown in panels (i) and (j) for agar and kiwi regions, respectively, do suggest improved precision in the images acquired with nonlinear gradients.

Finally, to probe quantitative ADC agreement, experiments were performed on the High-Precision Device (HPD) diffusion phantom shown in Fig. 8a. A summary of those results is shown in Fig. 8b. For vials 10 and 11, even with a gradient duration of 42ms
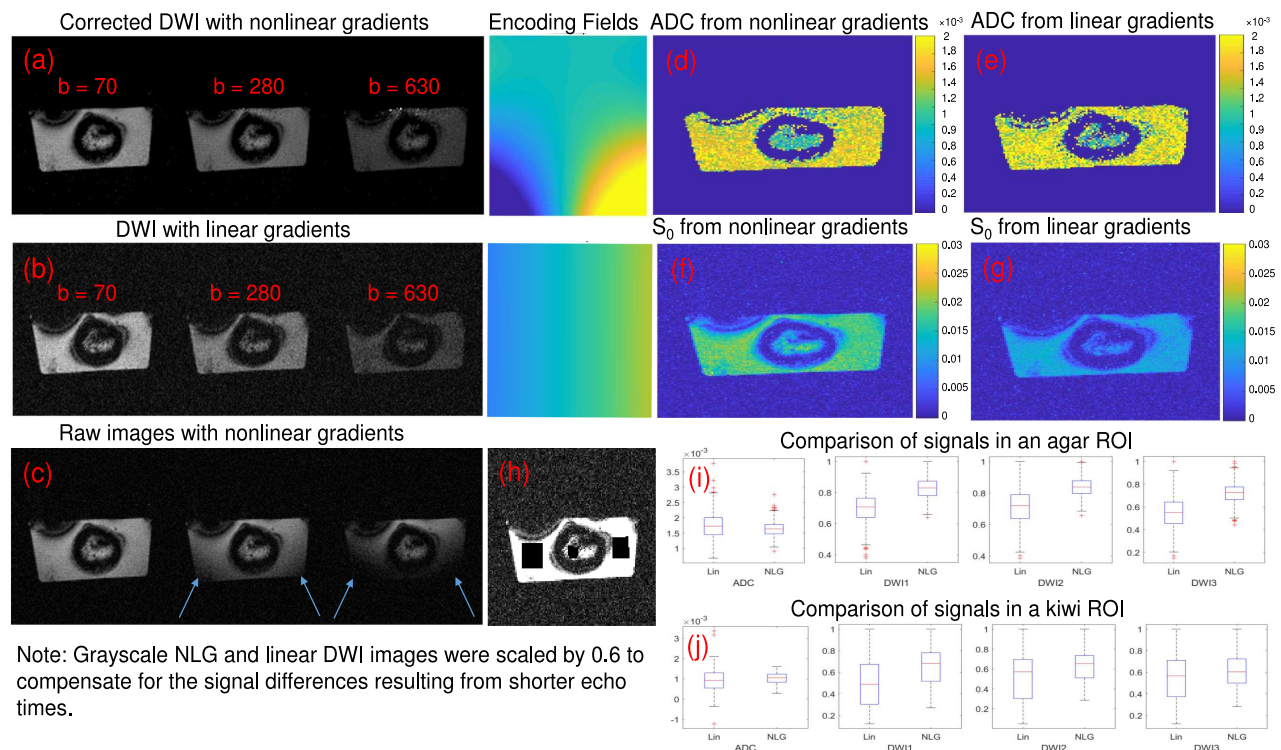
Figure 7: Experimental results from DWI with nonlinear and linear gradients. Panel (a) shows DWI images using a nonlinear C3 gradient and scaled to a uniform b-value. Standard images acquired by using linear gradients at these b-values (b) are shown for comparison and show excellent agreement. In the raw NLG images (c), the nonuniform diffusion weighting can be observed in the corners highlighted by blue arrows. Fitting this data to a monoexponential model yields ADC maps (d) that are in good agreement with those from linear gradients (e). Mapping S_0 from these monoexponential fits (f,g) shows that the shorter echo time afforded by nonlinear gradients results in about a doubling of signal. Furthermore, a comparison of image uniformity over the ROIs shown in (h) suggests the higher SNR of nonlinear DWI translates to better precision (i,j).

310   (TE=98), the maximum b-values were less than 200s/mm^2, so ADC could not be accurately

311   calculated. However, for the remaining vials, ADC agreement was very high. In these

312   studies, because of the phantom geometry and the shape of the field, most of the vials

313   required longer gradient durations for nonlinear gradient experiments. Thus, SNR of the

314   underlying images and accuracy of the measured ADC was not necessarily better. However,

315   these results provide reassurance that the diffusion contrast from nonlinear gradients closely

316   matches that of linear gradients.
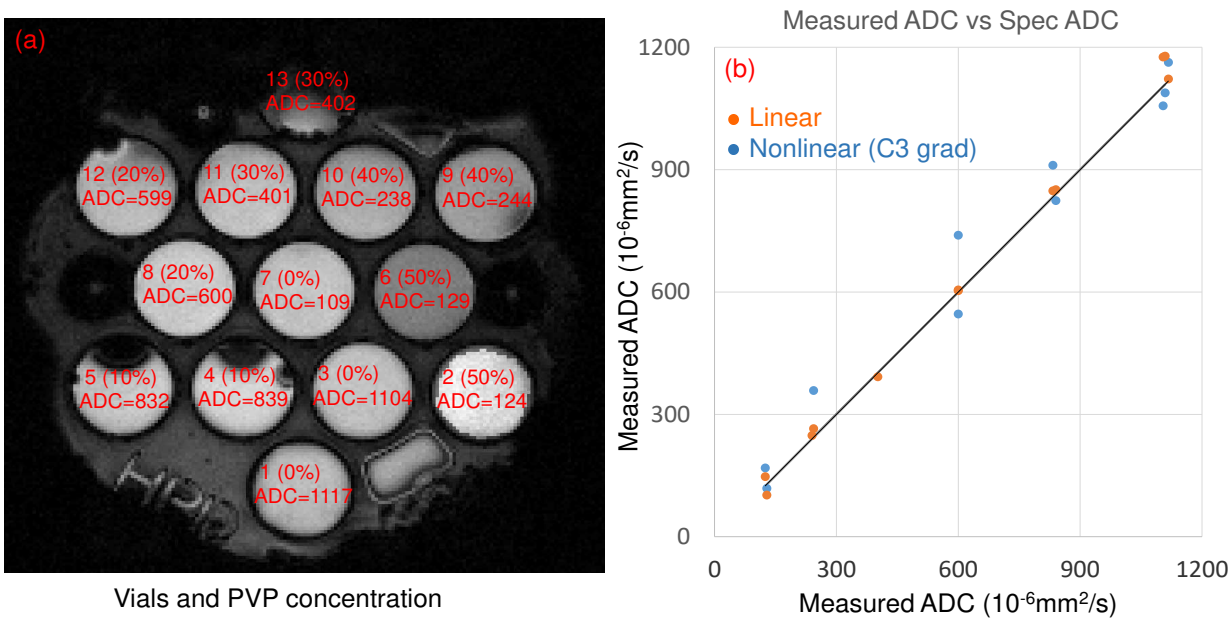
Figure 8: Quantitative comparisons of ADC in a diffusion phantom. (a) A diffusion phantom composed of vials of aqueous PVP (concentration in %) was used to test the agreement between ADC values measured with linear and nonlinear gradients. The three smaller 5mL vials are fiducial markers. (b) A comparison among measured ADCs shows good agreement.

IV.   Discussion

Because the device is meant only to deliver diffusion weighting, image encoding and reconstruction are unaffected. By focusing on $\| \nabla Bz \|$ over the anatomy of interest, the concept presented here could be comparable in price to other anatomically specific MRI accessories, such as RF coils, and be portable between scanners. Yet this accessory would deliver an order of magnitude increase in gradient strength and double contrast to noise ratios in prostate cancer detection.

The presented design shows that by abandoning design specifications required for imaging, particularly unidirectional linearity of the gradient and cylindrical geometry, the local magnitude and diffusion encoding can be greatly improved. Recently, this potential has also been explored in a volume-encompassing design for breast imaging[49]. Our experimental results show that nonlinear gradients can produce diffusion weighting that is qualitatively and quantitatively comparable to standard methods, even for phantoms whose geometry is

330 not particularly suited to the gradient topology. While current results focus on improved

331 ADC mapping, more sophisticated models of diffusion could also potentially be probed using

332 these much stronger imaging gradients[21–24,50–56].

333 Several features make this approach highly feasible with minimal changes to an existing

334 MRI system. Because diffusion waveforms for prostate DWI do not require a high degree

335 of flexibility, a dedicated DWI gradient would only require the addition of pulse sequence

336 synchronization pulses which then trigger a very simple waveform generator. Furthermore,

337 while initial implementations will feed these waveforms to a dedicated amplifier, a DWI

338 gradient of this kind could share the amplifier of one of the linear gradients via a switch.

339 In either case, the rest of the pulse sequence, including excitation with the body coil, image

340 encoding with linear gradients, reception with standard RF arrays, and Fourier transform

341 image reconstruction, proceeds unmodified. During the diffusion encoding module, the linear

342 gradients could either be turned off or run in tandem, to achieve still higher local gradient

343 or effectively move the region targeted for optimal diffusion weighting.

344 One concern with nonlinear gradients is the sensitivity of CNR to position. If the

345 prostate is too close to the device, there is higher gradient variability and additional DWI

346 images might be needed to get adequate diffusion encoding across the entire prostate. Alter-

347 nately, if the prostate is too far from the device, there may be concern that the gradient is

348 too weak to yield a significant benefit. While more sophisticated algorithms are possible for

349 optimizing gradient durations and amplitudes, the presented simulations show that even a

350 rudimentary algorithm for modifying Δ as a function of position can achieve very high CNR

351 for a range of anatomical placements.

352 Another consideration is whether the nonlinearity in the gradient affects the calculated

353 ADC value. In the present design, nonlinearity over a 1mm voxel with a median gradient

354 of 500mT/m contains deviations of approximately $\pm$10mT/m or 2%, but the effects of this

355 deviation partially cancel across the voxel[46]. This amount of gradient variation across a voxel

356 is comparable to that present in our experimental work, which achieved good agreement

357 using just the midpoint gradient value for the b-value of each voxel. However, more realistic

358 assignments of local b-value may show better performance.

359 In addition, the dependence of ADC values on TE, diffusion time and b-value is an ac-

360 tive area of research, and several models have been proposed. We have tried to address some

361 of these concerns by using a two-component model, which does impart b-value dependence
362 to the measured ADC. However, this cannot be entirely resolved with simulations, particu-
363 larly because the models are typically based on measurements with conventional hardware
364 that cannot access the short diffusion times achieved here. However, this type of device
365 could play an important role in further developing models that accurately characterize the
366 microstructure that contributes to DWI contrast[21–24].

367 For greater nonlinearity or higher-precision applications, it is also possible to derive
368 the diffusion equations for a nonlinear gradient. We have performed this analysis for the
369 simplest version of diffusion weighting, included in the supplementary material, which shows
370 that nonlinearity can lead to similarly small deviations in the calculated ADCs (O(1%)) that
371 depend on the ratio of linear and nonlinear field contributions in the field across a voxel. For
372 clinical applications, however, these corrections are never expected to be necessary. A greater
373 factor skewing ADC values is the dependence on encoding and echo times, which has been
374 demonstrated in human studies. However, stronger gradients only extend the potential to
375 characterize ADC as a function of time and TE. Encouragingly, clinical studies have already
376 shown that shorter encoding times improve the ability to distinguish cancerous and benign
377 prostate[21,22].

378 Like linear gradients, the proposed device could induce eddy currents during an echo-
379 planar imaging (EPI) readout. In the current experiments, long-lasting eddy currents were
380 not observed, and images were reconstructed via FFT without additional corrections. Fur-
381 thermore, the shorter echo times afforded by stronger gradients could potentially reduce the
382 distortions associated with EPI. However, more complicated and persistent fields could be
383 characterized via 2D phase-encoded mapping strategies, like those used to map dynamic
384 nonlinear gradient encodings[27,47,48]. Once known, linear and certain nonlinear components
385 could be physically compensated by appropriate waveforms, particularly since they need
386 only be compensated over the small ROI of the prostate and also because diffusion gradient
387 waveforms do not generally need to be changed with standard protocol changes. Finally,
388 since even standard "linear" gradients are not truly linear, modern eddy correction post-
389 processing techniques already model the observed eddy currents with a nonlinear basis[57].
390 With a change of basis, these same methods could be applied to the nonlinear gradient
391 presented here.

IV. DISCUSSION

392   Finally, while mechanical and thermal safety concerns were discussed in the Results, one
393   important safety concern may be the potential for peripheral nerve stimulation. Achievable
394   gradient moments in clinical imaging are often restricted by peripheral nerve stimulation
395   (PNS) limits on the slew rate, but those limits are based on studies with full body gradients.
396   More recent studies of PNS show that the overlap of anatomy with induced currents is the
397   real key to PNS stimulation, and due to their highly localized nature, nonlinear gradients
398   have long been hypothesized to produce less PNS for a given dB/dt[26,58]. Furthermore,
399   for this particular design, the most serious potential outcomes of PNS (i.e. stimulation of
400   currents across the heart) are avoided, since the field and gradient are very small at that
401   distance.

402   While true PNS limits are complex phenomena and will require additional testing for
403   confirmation, the geometry of this device also provides important new degrees of freedom
404   for mitigating PNS. In addition to lengthening ramp times, PNS can be further mitigated
405   by shifting device placement a few centimeters.

406   Fig. 9 in the supplementary material shows dB/dt assuming a 1ms ramp time for a
407   device placed 6cm inferior to the perineum. With this geometry, only a small volume of the
408   anatomy is subject to dB/dt greater than 20mT/m and, as shown in Fig. 5, CNR is still
409   approximately double of that achieved with standard linear gradients[59,60].
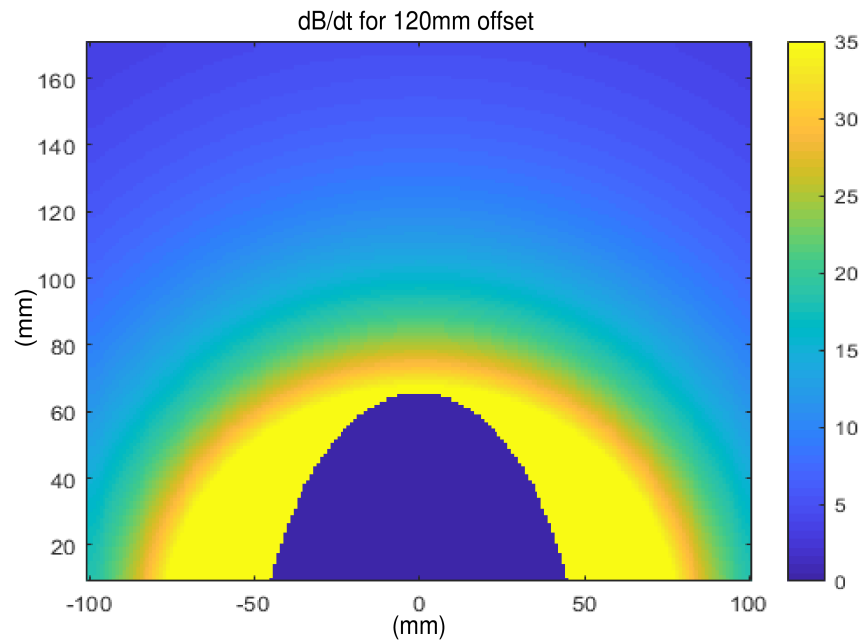
Figure 9: dB/dt for nonlinear gradient. Peripheral nerve stimulation is a complicated phenomenon which is made more difficult to predict in the presence of nonlinear gradients. However, one advantage of the hardware proposed here is that PNS can be mitigated by device placement. This plot shows dB/dt for a 1ms ramp time with an offset of 120mm from the prostate. The standard 20T/s slew is exceeded over a very small volume of the anatomy, reaching a maximum of 43T/s along the x=0 line, with reductions in leg stimulation achievable by spacers or positioning. Notably, simulations for this positioning (Fig. 5) show that CNR is still approximately twice what is achievable with linear gradients.

IV.   DISCUSSION

V.   Conclusion

410 We present a new approach to improving DWI of prostate, introducing a new type of MRI

412 accessory that delivers high diffusion weighting at short echo time, resulting in much stronger

413 gradients and higher SNR. Prostate is anatomically ideal for diffusion weighting via a non-

414 linear "inside-out" gradient, and the clinical significance and increasing ubiquity of prostate

415 MRI is likely to justify the additional hardware, which could be shared across many scan-

416 ners. Our results predict a doubling of CNR, which could improve the reliability of MRI for

417 prostate cancer imaging, which in turn could reduce both the high mortality and overtreat-

418 ment rates for this widespread disease.

Last edited $Date: September 22, 2020$

VI.   Appendix

VI.A.   Theory

The simplest calculation of diffusion weighting is to consider two infinitely short gradient pulses separated by a delay τ. To simplify notation and without loss of generality, we consider spin with initial location $x(t = 0) = \phi(t = 0) = 0$, so that $\Delta x = x$ and $\Delta \phi = \phi_0$. Over the delay, the spins have localized to a Gaussian distribution of positions,

$$P(x) = e^{-\frac{x^2}{\sigma^2}} \tag{2}$$

where σ is related to the rms distance travel in time τ. For linear gradients, G_l, after the refocusing gradient lobe, the phase of each spin depends on its positions at $t = \tau$, $\phi(t = \tau, x) \equiv \phi(x) = k_l \tau x = k_l x$ and $d\phi = k_l dx$. We can therefore calculate the ensemble average of magnetization M. Assuming uniform spin density, the ensemble average of M is proportional to the ensemble average of $e^{i\phi}$, which can be reformulated as an integral over x, as follows.

$$\left\langle e^{i\phi} \right\rangle \propto \int_{-\infty}^{\infty} P(\phi) e^{i\phi} d\phi = \int_{-\infty}^{\infty} e^{-\frac{x^2}{\sigma^2}} e^{ik_l x} k_l dx = k_l \sqrt{\pi} \sigma e^{-\frac{k_l^2 \sigma^2}{4}}. \tag{3}$$

The product $\sigma^2 k_l^2$ reflects gradient winding, diffusion time, and diffusion rate. Thus the exponent is analogous to the product $b \star \text{ADC}$ in the well-known Stejskal-Tanner equation[18]. Using the same simplified approach for a spin in the presence of both linear and a second order nonlinear field, the difference is in the relationship between ϕ and x: $\phi(t = \tau, x) \equiv \phi(x) = G_l \tau x + G_{nl} \tau x^2 = k_l x + k_{nl} x^2$ and $d\phi = (k_l + 2k_{nl} x) dx$ Now the integral to be evaluated is,

$$\left\langle e^{i\phi} \right\rangle \propto \int_{-\infty}^{\infty} P(\phi) e^{i\phi} d\phi = \int_{\infty}^{-\infty} e^{\frac{-x^2}{\sigma^2}} e^{i(k_l x + k_{nl} x^2)} (k_l + 2k_{nl} x) dx. \tag{4}$$

Using standard formulas, we obtain

$$\left\langle e^{i\phi} \right\rangle = k_l \left(\frac{\sqrt{\pi} \sigma}{\sqrt{1 - \sigma^2 k_{nl}}} e^{-\frac{k_l^2 \sigma^2}{4(1 - i\sigma^2 k_{nl})}} \right) + 2k_{nl} \left(\frac{\sqrt{\pi} i k_l}{2} \left(\frac{\sigma^2}{(1 - i\sigma^2 k_{nl})} \right)^{3/2} \right) e^{-\frac{k_l^2 \sigma^2}{4(1 - i\sigma^2 k_{nl})}}. \tag{5}$$

VI.   APPENDIX

442   Rearranging, one can obtain:

$$\left\langle e^{i\phi} \right\rangle = k_l \sqrt{\pi} \sigma e^{-\frac{\sigma^2 k_l}{4(1-i\sigma^2 k_{nl})}} \left(\frac{1}{\sqrt{(1-i\sigma^2 k_{nl})}} + \frac{ik_{nl}\sigma^2}{(1-i\sigma^2 k_{nl})^{3/2}} \right). \tag{6}$$

444   Simplifying and removing complex values from the denominators, this becomes:

$$\left\langle e^{i\phi} \right\rangle = k_l \sqrt{\pi} \sigma e^{-\frac{k_l^2 \sigma^2}{4(1+\sigma^4 k_{nl}^2)}} e^{-\frac{i\sigma^4 k_{nl} k_l^2}{4(1+\sigma^4 k_{nl}^2)}} \left(\frac{\sqrt{1+i\sigma^2 k_{nl}}}{\sqrt{1+\sigma^4 k_{nl}^2}} + \frac{ik_{nl}\sigma^2(1+i\sigma^2 k_{nl})^{3/2}}{(1+\sigma^4 k_{nl}^2)^{3/2}} \right) \tag{7}$$

446   As expected, when k_{nl} is zero this matches the linear gradient expression. More, gener-
447   ally, neglecting nonlinear winding will cause a slight underestimation of the effective diffusion
448   weight, which will lead to a slight overestimation of ADCs by a scaling factor of $(1+\sigma^4 k_{nl}^2)$.
449   This could bias ADCs by a few percent, if not corrected. The imaginary term in the ex-
450   ponent indicates that nonlinear winding can also add a periodic phase shift in the signal,
451   similar to what is observed with dephasing under a nonlinear gradient[41].

452   The complex factor in braces can alter both the magnitude and phase of the signal,
453   in principle. However, in practice $\sigma \approx 10^{-2}$cm and $k_{nl} \approx 10^2$-10^3Hz/cm^2, over which the
454   magnitude of this term ranges from 1 to 0.993 and its phase changes by less than 9 degrees.
455   These corrections are highly unlikely to have clinical significance even in high precision work.

456   # Acknowledgment

457   The authors gratefully acknowledge the efforts of Xavier Mooney, Ben Leigh, and Steve
458   Bates at Tesla Engineering Ltd., for providing initial design specifications. Advice by Terry
459   Nixon of the Yale Magnetic Resonance Research Center was also extremely helpful and is
460   greatly appreciated.

References

1   Key   Statistics   for   Prostate   Cancer.   American   Cancer   Society.
    https://www.cancer.org/cancer/prostate-cancer/detection-diagnosis-staging/acs-
    recommendations.html. Accessed 2020.

2   Brawley OW. Trends in Prostate Cancer in the United States. *J Natl Cancer Inst*
    Monogr. 2012;45:152-156. doi:10.1093/jncimonographs/lgs035.

3   Rawla P. Epidemiology of Prostate Cancer. *World J Oncol.* 2019;10(2):63-89.
    https://doi.org/10.14740/wjon1191.

4   Klotz L, "Prostate cancer overdiagnosis and overtreatment. *Curr Opin Endocrinol Dia-*
    *betes Obes.*2013;20(3):204-209. doi:10.1097/MED.0b013e328360332a.

5   Loeb S, Bjurlin MA, Nicholson J, et al. Overdiagnosis and Overtreatment of prostate
    cancer. *Eur Urol.* 2014;65(6):1046-1055. doi:10.1016/j.eururo.2013.12.062.

6   Ahmed HU, El-Shater AB, Brown LC, et al. Diagnostic accuracy of multi-parametric
    MRI and TRUS biopsy in prostate cancer (PROMIS): a paired validating confirmatory
    study. *Lancet* 2017:389(10071):815-822. doi:10.1016/S0140-6736(16)32401-1.

7   Algohary A, Viswanath S, Shiradkar R, et al. Radiomic Features on MRI Enable Risk
    Categorization of Prostate Cancer Patients on Active Surveillance: Preliminary Find-
    ings. *J. Magn. Reson. Imaging* 2018;48(3):818-828. doi: 10.1002/jmri.25983.

8   Weinreb JC, Barentszb JO, Choykec PL, et al. PI-RADS Prostate Imaging-
    Reporting and Data System: 2015. *Version 2. Eur Urol.* 2016;69(1):16-40.
    doi:10.1016/j.eururo.2015.08.052.

9   Padhani AR, Liu G, Koh DM, et al. Diffusion-Weighted Magnetic Resonance Imaging as
    a Cancer Biomarker: Consensus and Recommendations. *Neoplasia* 2009;11(2):102-125.
    doi:10.1593/neo.81328.

10 deSouza NM, Riches SF, Vanas NJ, et al. Diffusion-weighted magnetic resonance imag-
    ing: a potential non-invasive marker of tumour aggressiveness in localized prostate can-
    cer. *Clin Radiol.* 2008;63(7):774-782. doi:10.1016/j.crad.2008.02.001.

489 11 van Leeuwen PJ, Hayen A, Thompson JE, et al. A multiparametric magnetic resonance
490   imaging-based risk model to determine the risk of significant prostate cancer prior to
491   biopsy, BJU Int, 2017;120(6):774-481. doi: 10.1111/bju.13814.

492 12 Johnson LM, Turkbey B, Figg WD, et al. Multiparametric MRI in prostate cancer
493   management. *Nat Rev Clin Oncol.* 2014;11(6):346-353. doi:10.1038/nrclinonc.2014.69.

494 13 Mehralivand S, Shih JH, S. Rais-Bahrami S, et al. A Magnetic Resonance Imaging-Based
495   Prediction Model for Prostate Biopsy Risk Stratification. *JAMA Oncol.*;4(5):678-685.
496   doi:10.1001/jamaoncol.2017.5667.

497 14 Kasivisvanathan V, Antti SR, Borghi M, et al. MRI-Targeted or Standard
498   Biopsy for Prostate-Cancer Diagnosis. *N Engl J Med.* 2018;378(19):1767-1777.
499   doi:10.1056/NEJMoa1801993.

500 15 Siddiqui MM, Rais-Bahrami S, Turkbey B, et al. Comparison of MR/ultrasound fusion-
501   guided biopsy with ultrasound-guided biopsy for the diagnosis of prostate cancer. *JAMA.*
502   2015;313(4):390-397. doi:10.1001/jama.2014.17942.

503 16 Muller BG, Shih JH, Sankineni S, et al. Prostate cancer: interobserver agreement and
504   accuracy with the revised Prostate Imaging Reporting and Data System at multipara-
505   metric MR imaging. *Radiology* 2015;277(3):741-750. doi:10.1148/radiol.2015142818.

506 17 Callaghan PT. Structural Imaging Using q-Space. *Principles of Nuclear Magnetic Res-
507   onance Microscopy.* New York: Oxford University Press Inc.; 1991. 400-405 p.

508 18 Stejskal EO, Tanner JE, "Spin diffusion measurements: Spin echoes in the
509   presence of a time-dependent field gradient. *J Chem Phys.* 2004;42(1):288-292.
510   https://doi.org/10.1063/1.1695690.

511 19 Rosenkrantz AB, Chandarana H, Hindman N, et al. Computed diffusion-weighted imag-
512   ing of the prostate at 3 T: impact on image quality and tumour detection. *Eur Radiol.*
513   2013;23:3170-3177. doi:10.3348/kjr.2018.19.5.832

514 20 Chatterjee A, Watson G, Myint E, et al. Changes in Epithelium, Stroma, and Lu-
515   men Space Correlate More Strongly with Gleason Pattern and Are Stronger Predictors

516   of Prostate ADC Changes than Cellularity Metrics. *Radiology.* 2015;277(3):751-762.
517   doi:10.1148/radiol.2015142414.

518 [21] Lemberskiy G, Rosenkrantz AB, Veraart J, et al. Time-Dependent Diffusion in Prostate
519   Cancer.*Investigative Radiology* 2017;52(7):405-411. doi:10.1097/RLI.0000000000000356.

520 [22] Lemberskiy G, Fieremans E, Veraart J, et al. Characterization of Prostate Mi-
521   crostructure Using Water Diffusion and NMR Relaxation. *Front. Phys.* 2018;6:91.
522   https://doi.org/10.3389/fphy.2018.00091.

523 [23] Gilani N, Malcolm P, and Johnson G. A Model Describing Diffusion in Prostate Cancer.
524   *Magn Reson Med.* 2016;78(1):316-326. doi:10.1002/mrm.26340.

525 [24] Panagiotaki E, Chan RW, Dikaios N, et al. Microstructural Characterization of Nor-
526   mal and Malignant Human Prostate Tissue With Vascular, Extracellular, and Re-
527   stricted Diffusion for Cytometry in Tumours Magnetic Resonance Imaging. *Invest Radiol.*
528   2015;50(4):218-227. doi:10.1097/RLI.0000000000000115.

529 [25] Ito S, Yamada Y. Alias-free image reconstruction using Fresnel transform in the
530   phase-scrambling Fourier imaging technique. *Magn Reson Med.* 2008;60(2):422-430.
531   doi:10.1002/mrm.21672.

532 [26] Hennig J, Welz AM, Schultz G, et al. Parallel imaging in non-bijective, curvilinear
533   magnetic field gradients: a concept study. *Magnetic Resonance Materials in Physics,*
534   *Biology and Medicine* 2008;21(1):5-14. doi:10.1007/s10334-008-0105-7.

535 [27] Stockmann JP, Galiana G, Tam L, et al. In vivo O-Space imaging with a dedicated 12
536   cm Z2 insert coil on a human 3T scanner using phase map calibration. *Magn Reson Med.*
537   2013;69(2):444-455. doi:10.1002/mrm.24282.

538 [28] Galiana G, Stockmann JP, Tam L, et al. The role of nonlinear gradients in par-
539   allel imaging: A k-space based analysis. *Concepts in Magnetic Resonance Part A.*
540   2012;40A(5):253-267. doi:10.1002/cmr.a.21243.

541 [29] Hidalgo-Tobon SS, Theory of Gradient Coil Design Methods for Magnetic Res-
542   onance Imaging. Concepts in Magnetic Resonance Part A 2010;36A(4):223-242.
543   doi:10.1002/cmr.a.20163.

544 30 Setsompop K, Kimmlingen R, Eberlein E, et al. Pushing the limits of in vivo
545   diffusion MRI for the Human Connectome Project. *Neuroimage.* 2013;80:220-233.
546   doi:10.1016/j.neuroimage.2013.05.078.

547 31 Murphy G, Haider M, Ghai S, et al. The expanding role of MRI in prostate cancer. *AJR*
548   *Am J Roentgenol.* 2013;201(6):1229-1238. doi:10.2214/AJR.12.10178.

549 32 Hadaschik B. [Paradigm shift in urology: Prostate cancer diagnosis using MRI-targeted
550   or standard transrectal ultrasonography-guided biopsy]. *Urologe A.* 2018;57(6):727–728.
551   doi:10.1007/s00120-018-0668-5.

552 33 Merrett C, Mannas M, Black PC, et al. Magnet Before the Needle Commentary on:
553   MRI-targeted or Standard Biopsy for Prostate-cancer Diagnosis (PRECISION Trial).
554   *Urology* 2018;118:1-2. doi:10.1016/j.urology.2018.04.024.

555 34 Mowatt G, Scotland G, Boachie C, et al. The diagnostic accuracy and cost-effectiveness
556   of magnetic resonance spectroscopy and enhanced magnetic resonance imaging tech-
557   niques in aiding the localisation of prostate abnormalities for biopsy: a systematic re-
558   view and economic evaluation. *Health Technology Assessment* 2013;17(20):vii-xix, 1-281.
559   doi:10.3310/hta17200.

560 35 de Rooij M, Crienen S, Witjes JA, et al. Cost-effectiveness of magnetic resonance (MR)
561   imaging and MR-guided targeted biopsy versus systematic transrectal ultrasound-guided
562   biopsy in diagnosing prostate cancer: a modelling study from a health care perspective.
563   *Eur Urol.* 2013;66(3):430-436. doi:10.1016/j.eururo.2013.12.012.

564 36 R. Renard-Penna R, O. Rouvière O, P. Puech P, et al. Current practice and ac-
565   cess to prostate MR imaging in France. *Diagn Interv Imaging* 2016;97(11):1125-1129.
566   doi:10.1016/j.diii.2016.06.010.

567 37 Venderink W, Govers TM, de Rooij M, et al. Cost-Effectiveness Comparison of
568   Imaging-Guided Prostate Biopsy Techniques: Systematic Transrectal Ultrasound, Di-
569   rect In-Bore MRI, and Image Fusion. *AJR Am J Roentgenol.* 2017;208(5):1058-1063.
570   doi:10.2214/AJR.16.17322.

571   38   Mueller-Lisse UG, Murer S Mueller-Lisse UL, et al. Everyman's prostate phantom: kiwi-
572   fruit substitute for human prostates at magnetic resonance imaging, diffusion-weighted
573   imaging and magnetic resonance spectroscopy. Eur Radiol 2017;27(8):3362-3371.

574   39   Jendoubi S, Wagner M, Montagne S, et al. MRI for prostate cancer: can computed
575   high b-value DWI replace native acquisitions? European Radiology 2019;29:5197-5204.
576   https://doi.org/10.1007/s00330-019-06085-z.

577   40   High Precision Devices, Inc., 4601 Nautilus Ct S Boulder, CO 80301 USA.
578   https://doi.org/10.1007/s00330-016-4706-7.

579   41   Wagner F, Laun FB, Kuder TA, Mlynarska A, Maier F, Faust J, et al. Temperature and
580   concentration calibration of aqueous polyvinylpyrrolidone (PVP) solutions for isotropic
581   diffusion MRI phantoms. PLoS ONE 2017;12(6). https://doi.org/10.1371/journal.

582   42   Jensen JH, Helpern JA, Ramani A, et al. Diffusional kurtosis imaging: the quantification
583   of non-Gaussian water diffusion by means of magnetic resonance imaging. *Magn Reson
584   Med.* 2005;53(6):1432–1440. doi.org/10.1002/mrm.20508.

585   43   Si Y, Liu RB. Diagnostic Performance of Monoexponential DWI Versus Diffusion Kur-
586   tosis Imaging in Prostate Cancer: A Systematic Review and Meta-Analysis. *AJR Am J
587   Roentgenol.* 2018;211(2):358-368. doi:10.2214/AJR.17.18934.

588   44   Stockmann JP, Ciris PA, Galiana G, et al. O-Space imaging: Highly efficient parallel
589   imaging using second-order nonlinear fields as encoding gradients with no phase encod-
590   ing. *Magn Reson Med.* 2010;64(2):447-456. doi:10.1002/mrm.22425.

591   45   Tam LK, Stockmann JP, Galiana G, et al. Null Space Imaging: Nonlinear Mag-
592   netic Encoding Fields Designed Complementary to Receiver Coil Sensitivities for
593   Improved Acceleration in Parallel Imaging. *Magn Reson Med.* 2011;68(4):1166-1175.
594   doi:10.1002/mrm.24114.

595   46   Galiana G, Stockmann JP, Tam LK, et al. Spin dephasing under nonlinear gradients:
596   implications for imaging and field mapping. *Magn Reson Med.* 2012;67(4):1120-1126.
597   doi:10.1002/mrm.23085.

598 47 Wang H, Tam LK, Constable RT, et al. Fast rotary nonlinear spatial acquisition (FRON-
599   SAC) imaging. *Magn Reson Med.* 2016;75(3):1154-1165. doi:10.1002/mrm.25703.

600 48 Dispenza NL, Littin S, Zaitsev M, et al. Clinical Imaging Potential of FRONSAC. *Nature*
601   *Scientific Reports* 2019;9(1):1912. doi:10.1038/s41598-018-36802-5.

602 49 Littin S, Feng Jia F, Amrein P, et al. Single channel non-linear breast gradient coil for
603   diffusion encoding. Proc. Intl. Soc. Mag. Reson. Med. 28 (2020).

604 50 Wetter A, Nensa F, Lipponer C, et al. High and ultra-high b-value diffusion-weighted
605   imaging in prostate cancer: a quantitative analysis. *Acta Radiol.* 2018;56(8):1009-
606   1010doi:10.1177/0284185114547900.

607 51 Woodfield CA, Tung GA, Grand DJ, et al. Diffusion-Weighted MRI of Peripheral
608   Zone Prostate Cancer: Comparison of Tumor Apparent Diffusion Coefficient With
609   Gleason Score and Percentage of Tumor on Core Biopsy. *AJR Am J Roentgenol.*
610   2010;194(4):W316-W322. doi:10.2214/AJR.09.2651.

611 52 Hurrell SL, McGarry SD, Kaczmarowski A, et al. Optimized b-value selection for the
612   discrimination of prostate cancer grades, including the cribriform pattern, using diffusion
613   weighted imaging. *J. Med. Imag.* 2017;5(1):011004. doi:10.1117/1.JMI.5.1.011004.

614 53 Rosenkrantz AB, Parikh N, Kierans AS, et al. Prostate Cancer Detection Using Com-
615   puted Very High b-value Diffusion-weighted Imaging: How High Should We Go? *Acad*
616   *Radiol.* 2016;23(6):704-711. doi:10.1016/j.acra.2016.02.003.

617 54 Ueno Y, Takahashi S, Ohno Y, et al. Computed diffusion-weighted MRI for prostate can-
618   cer detection: the influence of the combinations of b-values. *Br J Radiol.* 2015;88(1048):
619   20140738. doi: 10.1259/bjr.20140738 [online].

620 55 Metens T, Miranda D, Absil J, et al. What is the optimal b value in diffusion-
621   weighted MR imaging to depict prostate cancer at 3T?. *Eur Radiol* 2012;22:703–709.
622   https://doi.org/10.1007/s00330-011-2298-9.

623 56 Liss MA, White NS, Parsons JK, et al. MRI-Derived Restriction Spectrum Imaging Cel-
624   lularity Index is Associated with High Grade Prostate Cancer on Radical Prostatectomy
625   Specimens. *Front Oncol.* 2015;5(30). doi:10.3389/fonc.2015.00030.

57   Andersson JLR, Sotiropoulos SN. An integrated approach to correction for off-resonance effects and subject movement in diffusion MR imaging. *NeuroImage.* 2016;15(125):1063-1078. doi:10.1016/j.neuroimage.2015.10.019.

58   Davids M, Guérin B, Malzacher M, Schad LR, Wald LL. Predicting Magnetostimulation Thresholds in the Peripheral Nervous System Usign Realistic Body Models. *Scientific Reports.* 2017;7(1):5316. doi:10.1038/s41598-017-05493-9.

59   A Primer on Medical Device Interactions with Magnetic Resonance Imaging Systems. *wwfdagov/MedicalDevices/DeviceRegulationandGuidance/GuidanceDocuments/ucm107721htm.* Accessed 2009.

60   Submission of Premarket Notifications for Magnetic Resonance Diagnostic Devices: Guidance for Industry and Food and Drug Administration Staff. In: FDA DoRH, ed. 2016.